Experimental investigation of the turbulent wake past real seabed elements for velocity variations characterization in the water column.

Maria Ikhennicheu, Grégory Germain, Philippe Druault, Benoît Gaurier

Experimental investigation of the turbulent wake past real seabed elements for velocity variations characterization in the water column.

Maria Ikhennicheu [1a], Grégory Germain[a], Philippe Druault[b], Benoît Gaurier[a]

[a] *Ifremer, Marine Structure Laboratory, 150 Quai Gambetta 62200 Boulogne sur Mer, France. gregory.germain@ifremer.fr*

[b] *Sorbonne Université, UPMC Univ Paris 06, CNRS, UMR 7190, Institut Jean Le Rond d'Alembert, F-75005 Paris, France. philippe.druault@sorbonne-universite.fr*

Abstract

In high flow velocity areas like those suitable for marine energy application, bathymetry variations create strong velocity fluctuations in the water column. It is therefore essential to characterize the turbulence evolution in the wake of seabed elements which may impact the loads on tidal turbines. For that purpose, experiments are carried out in a flume tank with R_e as high as achievable in Froude similitude, with bathymetry variations experimentally represented with various wall-mounted square elements of height H: a cylinder or a cube as unitary obstacles and combinations of these elements followed by an inclined floor to resemble smooth bathymetry changes. The onset flow is a simple boundary layer profile with height 1.3 H and a low turbulence intensity. PIV and LDV measurements are used to investigate the wake past all test cases in order to distinguish high floor elevation cases (unitary obstacles) from mean roughness effect (obstacle combinations). Results show that the obstacle combinations produce a wake less extended than for a single wide cylinder that produces an extended wake and very energetic turbulent events. With a single cube, no downstream development of large turbulent events exist and the wake reduces by a factor of 3 compared to the wake cylinder case. An inclined floor downstream of a single wall-mounted obstacle reduces its wake length but does not alter the turbulent structures shed. Turbulent velocity profiles extracted from every wake topology investigated are also compared. The general conclusion is that:

[1] Corresponding author. E-mail: maria.ikhennicheu@ifremer.fr

for small aspect ratio cases, the obstacle will not affect the water column. On the contrary, strong energetic turbulent events are emitted from large aspect ratio obstacles. Combinations cases stand in-between.

Keywords: Turbulence, Experimental trials, wall-mounted obstacles, PIV, LDV, marine energy

---

Nomenclature and Abbreviations

A_R	Aspect ratio
δ	Boundary layer thickness
δ_z	Boundary layer in the wake
D_e	Water depth
f_e	Sampling frequency
F_r	Froude number
g	Gravity
H	Rugosity height
$H_{in-situ}$	*In-situ* obstacle height
I	Turbulence intensity
l	Recirculation length
ν	Kinematic viscosity of water
S	Stagnation point
σ	Standard deviation
S_t	Strouhal number
τ_{uw}	Time-average Reynolds shear stress
U	Instantaneous streamwise velocity
$\overline{U}$	Time-average streamwise velocity
u'	Fluctuating streamwise velocity
$U_{in-situ}$	*In-situ* streamwise velocity
U_∞	Upstream time-average streamwise velocity
V	Instantaneous transverse velocity
$\overline{V}$	Time-average transverse velocity
v'	Fluctuating transverse velocity
W	Instantaneous vertical velocity
$\overline{W}$	Time-average vertical velocity
w'	Fluctuating vertical velocity
x	Streamwise position
y	Transverse position
$y0$	Symmetry plane: $y^* = 0$
$y1$	Transverse plane: $y^* = 1$
$y2$	Transverse plane: $y^* = 2$
z	Vertical position

1. Introduction

French waters are one of the largest tidal potential where industrial projects have started to emerge: it represents 25 % of the European potential [EDF (2010)]. In the Alderney Race, the flow presents currents up to $U_{insitu} = 5\ m/s$. In this kind of area, bathymetric variations are causing a high turbulence rate in the water column [Myers and Bahaj (2005)] and some very energetic turbulent events can rise up to the surface [Best (2005)]. Velocity fluctuations can have a major impact on the tidal turbines behaviour, on their production [Duràn Medina et al. (2017); Mycek et al. (2014)] and on the structural fatigue [Gaurier et al. (2013)]. It is therefore essential to characterize this kind of flow.

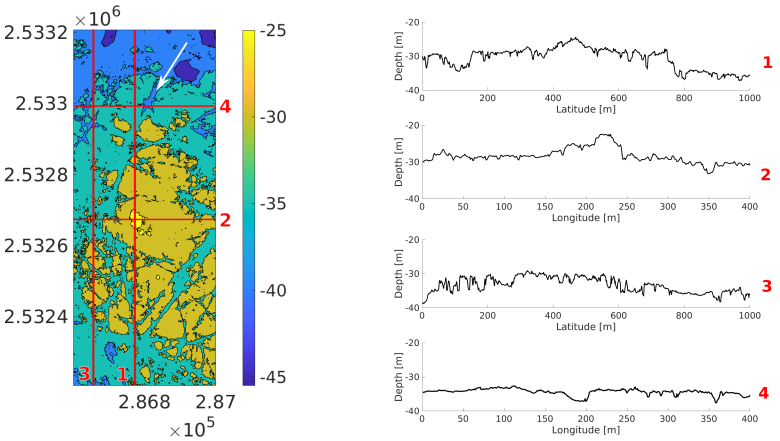

(a) Depth (colormap in m) in a 400 m × 1000 m area in the Alderney-Race. Axes are latitude (X-axis) and longitude (Y-axis) expressed in m

(b) Bottom elevation profiles at two locations in latitude and longitude

Figure 1: Bathymetry of the Alderney Race area [SHOM (2015)] where the mean flow direction is indicated with the white arrow.

Figure 1 illustrates bathymetry variations profiles in a $\sim 400\ m \times 1000\ m$ area of interest for tidal turbine application where three topology types can be identified. First, these profiles show an average bottom roughness with variations lower than 5 m (two bottom profiles in figure 1(b)) which can be experimentally represented with a combination of wall-mounted obstacles. Then, in some cases, high altitudes are detected, with an elevation of

$\sim 10\ m$ (two top profiles in figure 1(b)). These cases can be experimentally represented by unitary wall-mounted obstacles. Finally, in the top latitude profiles, smooth depth variations are visible. It will also be investigated through experimentations using floor inclination variations downstream of wall-mounted cubic elements.

Flow behaviour over bottom roughness *i.e* a combination of wall-mounted elements over large surfaces, has been extensively described in the literature, like in [Florens et al. (2013); Singh et al. (2016)]. A review on rough walls has been lead by [Jiménez (2004)] and the different behaviour between 2D and 3D roughness types is experimentally studied in [Volino et al. (2009)] at $R_e \sim 5 \times 10^4$ based on the roughness height. However these studies focus on the boundary layer development and not specifically on the wake past finite combination of obstacles. The combination of two or three identical wall-mounted elements has been studied, for example, in [Sakamoto and Haniu (1988); Martinuzzi and Havel (2000); Paik et al. (2009)]. They experimentally studied the impact on the wake of the spacing of two cubes or cylinders and showed a shift in the wake behaviour depending on the spacing. Nevertheless, the analysis of the combination of small amount of obstacles of various aspect ratios is rare in the literature.

In some areas, bathymetry shows an obstacle significantly higher than its neighbours (figure 1). Such obstacles can be experimentally represented with a unitary element: a single wall-mounted square obstacle like a cube or a cylinder. The wall-mounted cube is a common obstacle studied in wind tunnels or water tanks. [Hussein and Martinuzzi (1996); Martinuzzi and Tropea (1993)] are among the firsts to characterize the flow around a wall-mounted cube and to describe its wake. We also count the studies performed by [Castro and Robins (1977)] going up to $Re = 10^5$ or Hearst et al. [Hearst et al. (2016)] at $R_e = 1.8 \times 10^6$. Previous works [Ikhennicheu et al. (2018a)] also detailed the wake past a wall-mounted cube at high Reynolds number $R_e = 2.5 \times 10^5$. The effect of the addition of an inclined floor downstream of the cube has also been studied [Ikhennicheu et al. (2018a,b)]. Experimental results show that turbulent structures are impulsed higher than the simple floor translation, even if the floor inclination does not have an impact on the nature of turbulent structure emitted from the obstacle wake.

The impact of the aspect ratio (A_R = Width/Height) on the obstacle wake, has been experimentally studied by [Schofield and Logan (1990); Diabil et al. (2017); Martinuzzi and Tropea (1993)]. The latest, through experi-

mental analysis, found that for $A_R = 6$, the recirculation region downstream of the obstacle switches from a 3D aspect to a nominally 2D aspect. The aspect ratio impact on the wake development has also been investigated in [Ikhennicheu et al. (2018b)], showing that for an aspect ratio 7 times superior, the recirculation length triples and large coherent structures are detected in the wake.

The case of $A_R = \infty$ is a classical example of a 2D obstacle in the literature [Castro (1979); Liu et al. (2008)]. The latest characterized the wake of a rib at $R_e \sim 1.5 \times 10^4$. They found that at $x/H = 15.75$ downstream of the obstacle, the streamwise velocity is not fully recovered. However, at this location behind a 3D wall-mounted cube [Hearst et al. (2016)], the wake of the obstacle is fully dissipated as the wake is less impacted by side effect and thus extends. Finally, the experimental works of [Wang et al. (2009)] offer a topology of the fluid past a rib at $R_e = 2.2 \times 10^4$. However, few studies focus on the wake development of finite length square cylinder cases. Obstacle material is also of interest, especially the obstacle surface roughness. [Choi et al. (2008); Beratlis et al. (2018)] discuss the effects of the surface-roughness on the mean flow past bluff bodies and bumps (respectively). They show that the drag coefficient reaches a minimum value at a critical Reynolds number that decreases with increasing roughness. That aspect is not investigated in the present work where only smooth obstacles are investigated.

Few of the studies exposed in this bibliographic review present cases with $R_e > 10^5$. The Reynolds number, based on H_{insitu} and U_{insitu} is substantially high: $R_{e,insitu} = H_{insitu}U_{insitu}/\nu = 2.5 \times 10^7$, with $H_{in-situ} \sim 5\ m$ and ν the kinematic viscosity of water. It is generally assumed that, for $R_e > 4 \times 10^4$, the turbulent flow achieves a certain Reynolds number independency as found by [Castro and Robins (1977)]. However, that conclusion has been questioned in [Lim et al. (2007)] where it is explained that for vortex-dominated flows, mean flow is likely to be Re-dependent. Hence, there is a necessity to extend the existing database for marine energy application through high Reynolds number experiments. The present experiments are carried out at $R_e = 2.5 \times 10^5$, although 100 times lower than *in-situ* conditions, it offers a new set of results on high Reynolds number flows experiments.

In the present study, the wake past various wall-mounted cubic elements in a high Reynolds number flow is studied in order to elucidate the obsta-

cles wake extension and the vortex structures emission in the water column. First, the experimental set-up and velocimetry techniques are described. Bathymetry is divided into two main experimental representations. First, the description of the flow around unitary wall-mounted obstacle with low and large aspect ratios along with floor inclination variations is proposed. Then, the case of wall-mounted elements combinations representative of average bottom roughness is investigated. Their impact on the flow is analysed through spatial and spectral analysis. Finally, a discussion is proposed on the velocity profiles generated by the different wall-mounted elements likely to impact the tidal turbines.

2. Experimental set-up

2.1. The IFREMER *circulating tank*

Tests are carried out in the wave and current circulating flume tank of IFREMER located in Boulogne-sur-Mer (France) presented in figure 2. The incoming flow is assumed to be steady and constant. The test section is 18 m long $\times$ 4 m wide $\times$ 2 m deep. By means of a grid combined with a honeycomb (that acts as a flow straightener) placed at the inlet of the working section (see figure 3(a)), a low turbulent intensity of $I = 1.5$ % is achieved. In this work, the three instantaneous velocity components are denoted (U, V, W) along the (x, y, z) directions respectively (figure 3(a)).

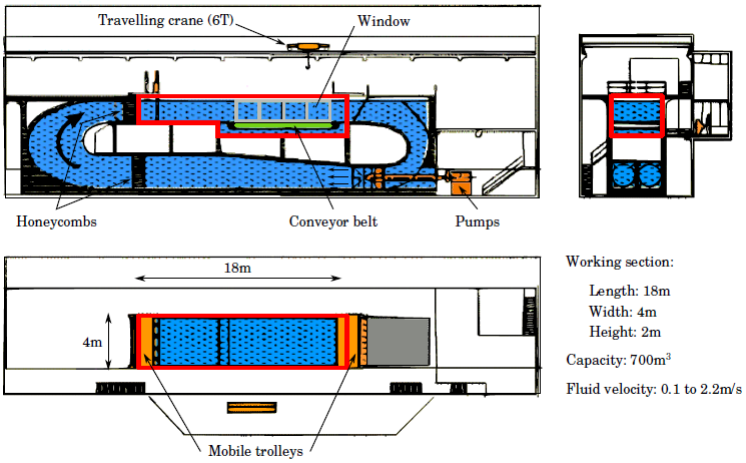

Figure 2: IFREMER Flume tank in Boulogne-sur-Mer.

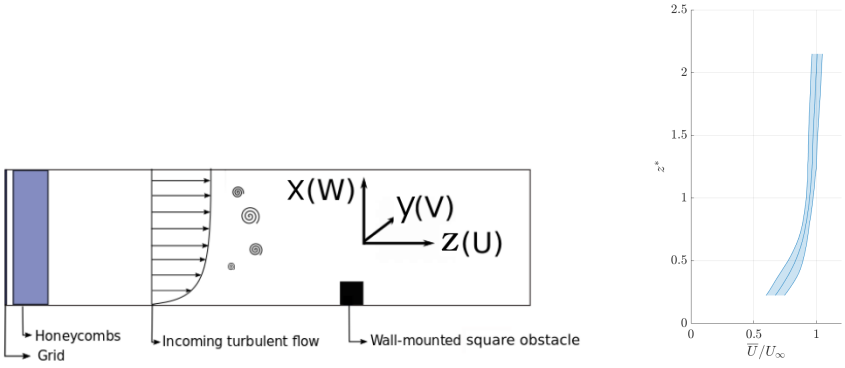

Figure 3: Schematic view of an obstacle in the wave and current circulating tank of IFREMER (left) and $\overline{U}$ profile 1.5 H upstream of the first obstacle with standard deviation for $I = 1.5$ % (right).

Using the Reynolds decomposition, each instantaneous velocity component is separated into a mean value and a fluctuation part: $U(X,t) = \overline{U(X)} + u'(X,t)$, where an overbar indicates the time average. In the following, the denoted Reynolds shear stress component corresponds to $\tau_{uw} = \overline{u'w'}$. Non dimensional lengths are used for all parameters indexed by *: $x^* = x/H$, for instance, with H the obstacle height. The velocity profile upstream of the obstacle is illustrated in figure 3(b). The boundary layer height δ^* is calculated as $\delta^*_{95} = z^*(\overline{U} = 0.95 \times \overline{U}_\infty) = 1.3$.

	U_∞ [m/s]	Rugosity height H [m]	Depth D_e [m]	$R_e = \frac{HU_\infty}{\nu}$	$F_r = \frac{U_\infty}{\sqrt{gD_e}}$
Alderney Race	5	5	40	2.5×10^7	0,25
Flume tank	1	0,25	2	2.5×10^5	0,23

Table 1: *In situ* and experimental conditions.

The experimental conditions are summed up in table 1. In order to consider turbulent events interaction with the free surface, experiments are achieved in Froude similitude F_r with g the gravity and D_e the water depth. Furthermore, Reynolds number must be as high as achievable to be closer to real conditions. It is also required to have a low ($< 10\%$) blockage ratio (obstacle frontal surface/tank section) in order to limit the tank side effects on the obstacle wake. Hence, for both cases of bottom roughness and unitary obstacles, we consider, to represent the average bathymetry elevation,

obstacles with a $H = 0.25\ m$ height.

In some cases, the seabed can present smooth depth variations. An average elevation of 12 m over 105 m can be measured in figure 1(b). This kind of elevation is experimentally reproduced with a 3 m long $\times 3$ m wide plane with an inclination of 6.5° in order to study the floor inclination effect on the wake behaviour.

2.2. Test cases

The square wall-mounted elements representative of *in-situ* obstacles investigated here are represented in figure 4 and additional top and side view are available in appendix. They are all made of plexiglas with no wall roughness and different aspect ratios are considered, representing various marine bathymetry variations. In order to elucidate the obstacle(s) wake development in the water column and to identify the emission and generation mechanism of vortex structure, six test cases are considered in this study: a cube and a cylinder alone in the flow, a combination of a cube followed by a cylinder, a cube and a cylinder followed by an inclined floor, and finally a cylinder followed by two cubes followed by a cylinder (respectively illustrated in figure 4).

Origin is set at the middle of the most downstream obstacle. Obstacles are disposed symmetrically around $y^* = 0$. Nomenclature is chosen as follows. C_n indicates a wall-mounted square obstacle (*i.e.* a cube or a cylinder), with n the aspect ratio: A_R = width/length. S_m indicates the inclined floor with m the inclination angle: $m = 6$ for a 6.5° angle. $C_n d^* S_m$ is a combination of obstacles where d^* is the spacing between consecutive obstacles, when $d^* = 0$, nothing is indicated. A square exponent indicates that two identical obstacles are disposed in the transverse direction. Hence, case $C_1 S_6$ is a cube directly followed by an inclined floor. Case $C_3 1 C_1^2 1 C_2$ is a cylinder of $A_R = 3$ spaced by H from two cubes spaced by H from a cylinder of $A_R = 2$.

Cases C_1 and C_7 are chosen as reference cases in order to describe the wake over canonical cases. $C_1 2 C_6$ is chosen to study the effect of the addition of an upstream perturbation on the cylinder wake development. The spacing is chosen to be the most critical for the cylinder wake development. Based on the works of [Martinuzzi and Havel (2000)], an intermediate spacing of 2 H is chosen. Case $C_3 1 C_1^2 1 C_2$ is a more complex case, different obstacles

are selected to represent a random bathymetry variation and spacing is the same between each row in order to have a similar interaction between each row.

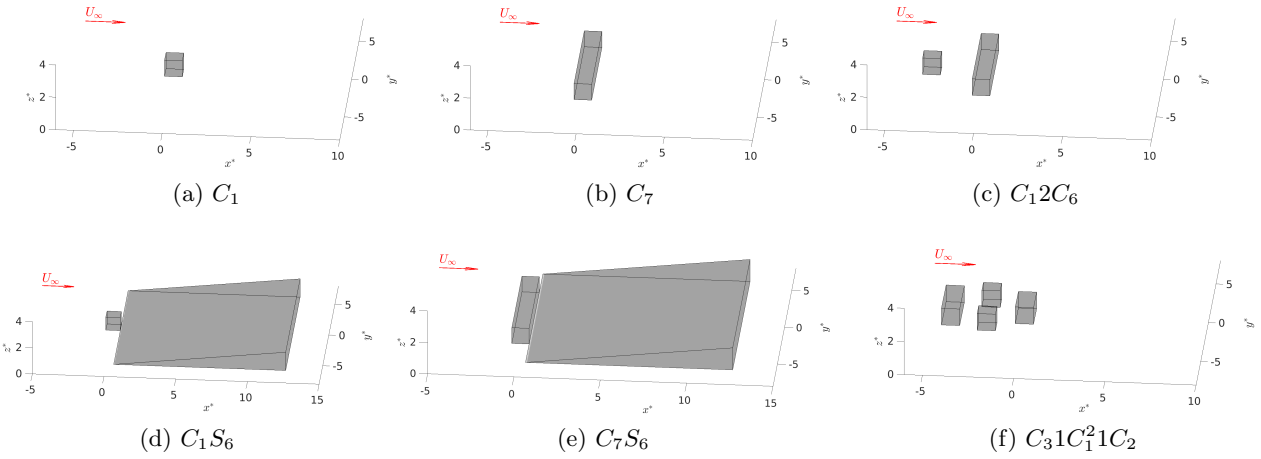

(a) C_1 (b) C_7 (c) $C_1 2 C_6$

(d) $C_1 S_6$ (e) $C_7 S_6$ (f) $C_3 1 C_1^2 1 C_2$

Figure 4: Schematic representation of obstacles combinations studied. (a) and (b) represent steep elevations, (c) and (f) average bottom roughness and (d) and (e) steep elevation with smooth depth variation.

2.3. PIV & LDV

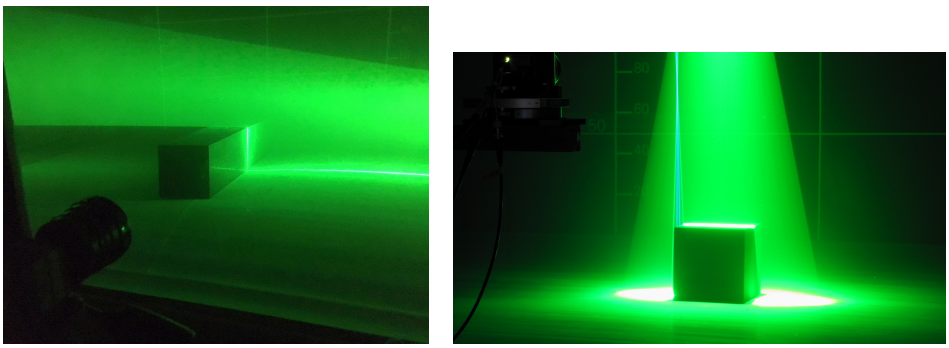

Figure 5: Pictures of obstacles in the tank. (left) the cylinder lighted with PIV laser sheet. (right) the cube lighted with PIV laser sheet and LDV laser beams.

Two Laser Velocimetry techniques are used to characterize the flow: LDV (Laser Doppler Velocimetry) and PIV (Particle Image Velocimetry):

see figure 5. Beforehand, the tank is seeded with 10 μm diameter silver coated glass particles. For the PIV measurements, a Nd-YAG Laser GEMINI-LIKE is used: power is 200 mJ per probe and wavelength is 532 mm. It is synchronized with a Camera FLOWSENS EO-2M 1600pix $\times$ 1200pix that makes double images with a time step of 800 μs for test cases C_1 and C_1S_6 and 1600 μs for every other test cases. Indeed, narrow angle lens are used for cases C_1 and C_1S_6 and wide angle lens for the rest and different focal requires a different time step. In these conditions, a particle is detected on 3 to 5 pixels, cross-correlation peak intensity is between 0.3 and 0.8 and peak detectability [Adrian and Westerweel (2011)] is 8 in average. PIV acquisitions are made for 150 s, with a 15 Hz acquisition frequency hence 2250 double images are acquired for all cases. The data are post processed with DYNAMIC STUDIO. Particles displacement is calculated using a Cross-Correlation [Meinhart et al. (1993)]. Outliers are then replaced with the Universal Outlier Detection [Westerweel and Scarano (2005)], example and precisions on that method can be found in [Ikhennicheu et al. (2019b)]. PIV measurements are carried out at various transverse positions: $y^* = 0$, $y^* = 1$ and $y^* = 2$ (denoted $y0$, $y1$ and $y2$ respectively) represented in figure 6. The laser lightens the $(y^* = 0, 1, 2)$ plane and the camera is positioned perpendicularly to the flow, next to the tank window. The camera is then moved for each measurement plane. Position of PIV planes depends on the wake topology. A list of PIV planes performed with measurements spatial discretization are summed up in table 2 and PIV measurement planes are illustrated in figure 7.

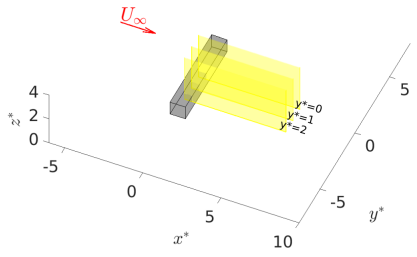

Figure 6: PIV measurements planes locations with $y^* = 0$ the symmetry plane.

The LDV measurements are made using a 2D DANTEC FIBERFLOW system. The probe is positioned horizontally for (U, V) measurements and and vertically for (U, W) measurements. The LDV measurements, acquisition frequencies are not constant, depending of the particles passing through

Case	Location	Field $[pix^2]$	Field $[mm^2]$	Discretization $[mm]$
C_1	$y^* = 0$	1600×1200	350×275	3.53
C_1S_6	$y^* = 0$	1600×1200	421×316	4.25
C_7 and C_7S_6	$y^* = 0$	1600×800	1162×581	11.7
C_6 and C_12C_6	$y^* = 0$	1600×600	1153×430	11.6
C_6 and C_12C_6	$y^* = 1$	1600×600	1250×470	12.6
C_6 and C_12C_6	$y^* = 2$	1600×600	1360×510	13.7
$C_31C_1^21C_2$	$y^* = 0$	1600×600	1140×425	11.5

Table 2: Characteristics of PIV measurement planes.

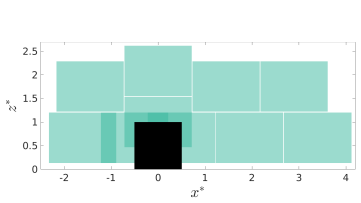

(a) C_1

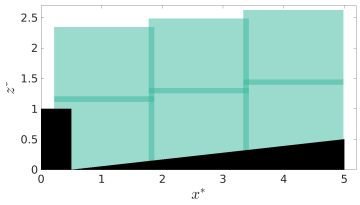

(b) C_1S_6

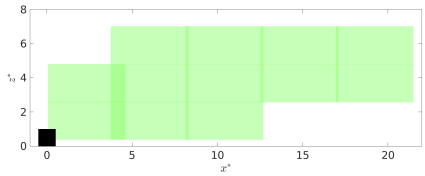

(c) C_7 and C_7S_6

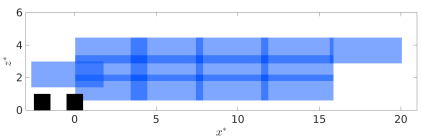

(d) C_12C_6 and C_6

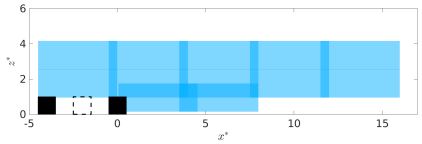

(e) $C_31C_1^21C_2$

Figure 7: PIV measurement planes locations in $y^* = 0$.

the measurement volume. At a given streamwise position, f_e varies from 70 to 270 Hz depending on the turbulent agitation. LDV signals (duration of 6 minutes) are re-sampled with a fixed sampling frequency f_e [Duràn Medina et al. (2015)]. Beforehand, fluctuating velocity signals are cut into blocks of 1024 points and a Fast Fourier Transform (FFT) is applied on every block. In the following, Power Spectrum Densities (PSD) are plotted versus the Strouhal number $S_t = fH/U_\infty$.

For the two measurement techniques, uncertainty is estimated to be around 2 % for LDV and 2.6 % for PIV, calculus are detailed in [Ikhennicheu et al. (2019b)].

3. Characterization of unitary wall-mounted obstacle wake

In-situ, elements higher than the average roughness are observed. For instance, in figure 1(b), a small hill is detected. It is approximately 10 m high, which is twice the average roughness. These elements are represented here with isolated wall-mounted cubic elements. In previous works, experimentations have been carried out on three different aspect ratio wall-mounted square obstacles: C_1, C_6 and C_7. This chapter gathers the results and gives general conclusions on the aspect ratio effect on the obstacle wake. In this study, the effect of an inclined floor representative of a smooth depth variation behind the cylinder is for the first time studied, as it has already been done for the cube in [Ikhennicheu et al. (2018a)].

3.1. Spatial analysis

In [Ikhennicheu et al. (2019b)], a comparison is made between two large aspect ratio cases: C_6 and C_7. Results showed that streamwise velocity profiles are very similar. The largest difference is measured for $x^* = 8$, $z^* = 1$ and is equal to 0.05 m/s. Indeed, [Martinuzzi and Tropea (1993)] showed that for $A_R \geq 6$, the recirculation region downstream of a square obstacle switches from a 3D aspect to a nominally 2D aspect and the evolution of the recirculation length is gentler. Hence, in the symmetry plane, it is assumed that cases C_6 and C_7 can be considered together as a large aspect ratio case C_L.

The wall-mounted cube alone case was extensively studied in the literature [Hearst et al. (2016); Hussein and Martinuzzi (1996); Martinuzzi and Tropea (1993)] and in previous works [Ikhennicheu et al. (2018a)]. Average streamwise velocity and Reynolds shear stress maps for the cube C_1 are presented in figure 8(a) and (b). It is compared to case C_L illustrated in figure 8(c) and (d). PIV plane borders suffer from poor lightning and data in these area are locally not fully converged, it is then chosen to cut off the sides of each measurement plane. For both cases, the flow separates at the leading edge of the obstacle and reattaches downstream with a well marked shear layer developing between the outer undisturbed flow and the recirculation region.

The recirculation lengths are $l^*(C_1) = 1.9$ and $l^*(C_L) = 6$, hence the recirculation bubble in the symmetry plane $y^* = 0$ triples. As explained by [Martinuzzi and Tropea (1993)], for obstacles with high A_R, the two ends of the horseshoe vortex are farther apart and have smaller influence on the

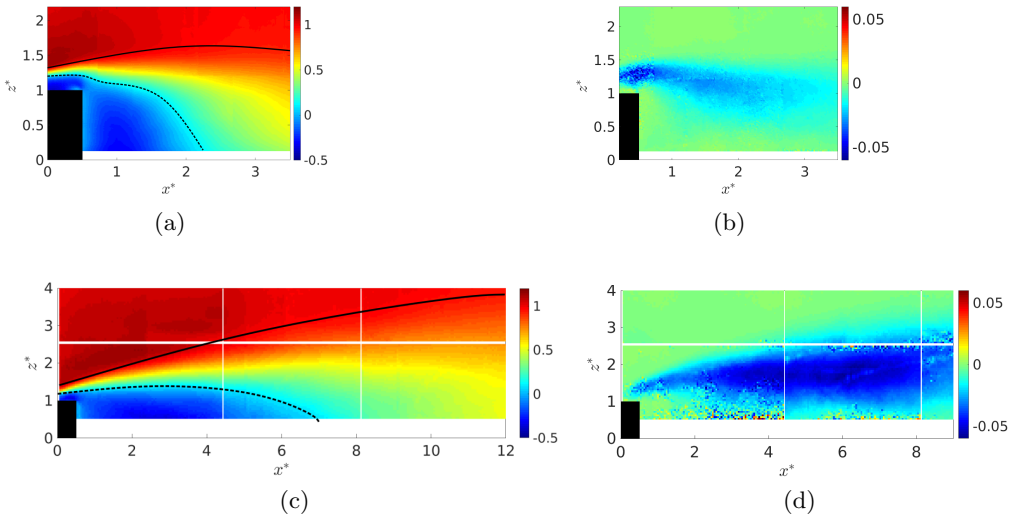

Figure 8: $\overline{U}$ (left) and τ_{uw} (right) maps for case C_1 (top) and C_L (bottom) in the symmetry plane $y0$. Full line is the wake extension ($\overline{U} = 0.9 * \overline{U}_\infty$) and dotted line marks out the recirculation area ($\overline{U} < 0$).

middle region of the wake, unlike for small A_R obstacles where they interact and cause a three dimensional behaviour of the wake. Additionally, the flow goes necessary over rather than around the obstacle. Both of these behaviour are causing the increase of the recirculation area and of the wake.

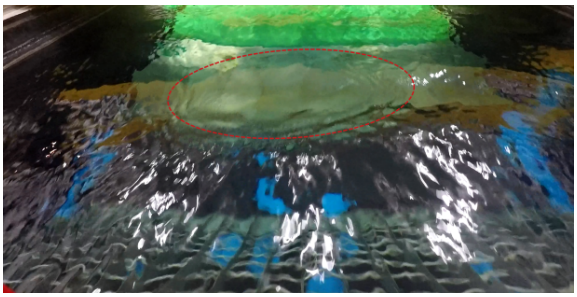

Figure 9: Picture of a boil of diameter $\sim 1\ m$ at the tank surface at $\sim 8\ m$ in the wake of a wall-mounted cylinder.

For test case C_L, large boils are observed at the tank surface, as illustrated in figure 9, while no boil is detected for every other cases. Turbulent structures emitted downstream of the cylinder are detected and tracked us-

ing PIV measurements in [Ikhennicheu et al. (2019b)] and an explanation for their creation is proposed. Kelvin-Helmholtz instabilities are generated in the wake of the obstacle. Then, as demonstrated in [Muller and Gyr (1987); Leweke et al. (1999)], these events interact to form hairpin structures [Diabil et al. (2017); Chaurasia and Thompson (2011)]. Hairpin structures are very energetic and can rise up in the water column and then erupt at the free surface creating a boil. These structures size is close to classical horizontal and vertical axis turbine diameters, hence they will be referred to as large scale turbulent structures. For further fatigue analysis on turbines, the question of the periodicity of turbulent events needs to be investigated through spectral analysis.

3.2. Spectral analysis

Spectral analysis is achieved on cases C_1 and C_L for two points at different positions using LDV measurements. As explained in section 2, LDV signals are re-sampled and a FFT is applied. More details on the LDV post-processing method can be found in [Ikhennicheu et al. (2019b)]. Results for all 3 velocity components are presented in figure 10 versus the Strouhal number $S_t = fH/U_\infty$ with f the frequency. Shedding peak, consistent with Kelvin-Helmholtz vortices, appears at $S_t = 0.07$ on u' and w' for case C_L and at $S_t = 0.09$ only on v' for case C_1. Those shedding peak values are within the range of values that can be found in the literature for a cube [Hearst et al. (2016); Hussein and Martinuzzi (1996)] and for a square cylinder [Omidyeganeh and Piomelli (2011)]. Turbulent events are then more frequent for smaller aspect ratio case C_1 but they are much smaller and less intense compared to case C_L [Ikhennicheu et al. (2018b)]. The differences observed in the spectral content of the different velocity component is a sign of a complex 3D vortex organisation in the flow. For test case C_L, the decrease of the spectra is steeper than the $-5/3$ slope, a representation of the Richardson-Kolmogorov cascade of energetic transfer in turbulence [Pope (2000)]. That is a sign of the non-isotropic aspect of the flow associated to 3D turbulent structures.

3.3. Floor slope effect

The cases considered so far are representative of blunt bathymetry variations. *In-situ*, smooth depth variations can be found. In this section, we

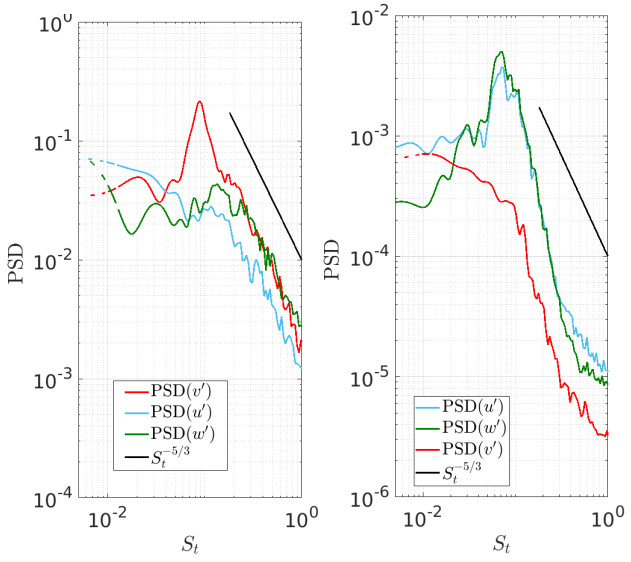

(a) C_1 (b) C_L

Figure 10: PSD velocity spectrum versus S_t of cases C_1 in $(x^* = 2, y^* = 0, z^* = 0.7)$ and C_L in $(x^* = 5, y^* = 0, z^* = 4)$: for u' (blue), v' (red) and w' (green).

study how the floor inclination impacts the wake and the large scale turbulent events described in previous section.

PIV measurements around case C_1S_6 show that the wake aspect (its length and orientation) is strongly influenced by the floor inclination as can be seen on figure 11 compared to figures 8(a) and 8(b). The main difference is the appearance of a stagnation point S [Ikhennicheu et al. (2018a)] at ($x^* = 1.7$, $z^* = 0.7$) located on the outline of the recirculation region. The appearance of S can be caused by the flow passing over and by the sides of the cube. Side vortices are driven towards the upper part of the water column by the inclined floor and they interact with the top vortex leading to the appearance of a stagnation point. Additionally, the recirculation region shortens : $l^*(C_1S_6) = 1.7$ compared to $l^*(C_1) = 1.9$. The inclined floor presence induces a blocking effect that squeezes the shear layer. Figure 11(b) also illustrates the shortening of the shear layer with the inclined floor: at $x^* = 3.5$, the shear layer is strongly reduced for case C_1S_6 and still persists for case C_1. In case C_1S_6, the floor inclination reorientates the shear layer towards the surface and it reaches higher altitude.

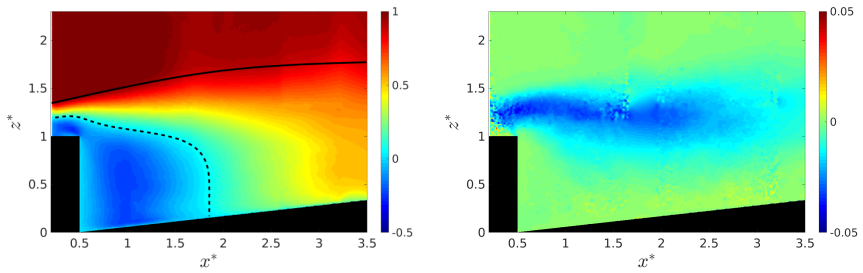

(a) (b)

Figure 11: Averaged map of $\overline{U}$ (a) and τ_{uw} (b) of case C_1S_6 in $y0$. Full line is the wake extension ($\overline{U} = 0.9 * \overline{U}_\infty$) and dotted line marks out the recirculation area ($\overline{U} < 0$).

Velocity maps are compared for cases C_L and C_LS_6 in figures 8(c), 8(d) and 12 (respectively). The inclined floor impact on the cylinder wake is similar to the cube case. Indeed, with the blocking effect of the floor inclination, the wake is redirected towards the surface and is thinner and shorter. Recirculation length reduces: for C_L, $l^* = 6$ and for C_LS_6, $l^* = 5.3$. For both test cases C_1 and C_L, the floor inclination reduces the recirculation length by 11 %. Spectral analyses were performed for C_L and C_LS_6 and are detailed in [Ikhennicheu et al. (2018b)]. It demonstrates that there is a small shift of the shedding peak between cases C_LS_6 and C_L. However, the inclined floor does not have an impact on the organisation of the structures being shed: large scale structures supposed to be hairpin vortex are created and large boils still form at the free surface for C_LS_6.

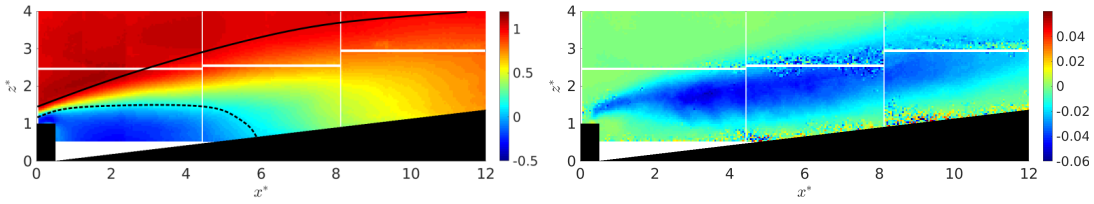

(a) (b)

Figure 12: Averaged map of $\overline{U}$ (a) and τ_{uw} (b) of case C_LS_6 in $y0$. Full line is the wake extension ($\overline{U} = 0.9 * \overline{U}_\infty$) and dotted line marks out the recirculation area ($\overline{U} < 0$).

3.4. Conclusion on unitary obstacle cases

The large aspect ratio wall-mounted cylinder produces a very extended wake and large scale turbulent structures are being shed from its shear layer. These structures can rise to the surface. A previous study shows [Ikhennicheu et al. (2019b)] that these vortices diameter is $\sim 0.35\ m$ which is about half the turbine diameter at this scale (1/20). Additionally to the high turbulence level, the wake induces a shear larger in the velocity profile impacting the turbine, as explained in [Ikhennicheu et al. (2019a)]. For the C_1 case, side effects impact the symmetry plane and the recirculation length reduces by a factor of 3 compared to the C_L case.

4. Rugosity sea-bottom cases

Previous section deals with single obstacles. However, they are rare cases. Most of the bathymetric variations are in combinations. To that purpose, two cases with arrangement of cubic elements are here considered ($C_1 2 C_6$ and $C_3 1 C_1^2 1 C_2$) in order to represent average bathymetry variations of 5 m.

4.1. Spatial analysis

In order to understand the interaction between obstacles and their impact on the water column,a cube is added upstream of the cylinder described in previous section and test case $C_1 2 C_6$ is investigated. The flow behaviour is presented in figure 13. The averaged shear stress map shows a strong shear behind the cube. Comparing to the cube alone case, the shear layer developing behind the cube is impulsed by the cylinder and reaches higher altitude in the symmetry plane: values of $\tau_{uw} < -0.05$ reach $z^* = 1.5$ in the C_1 case compared to $z^* = 2.7$ in the $C_1 2 C_6$ case. The cylinder presence promotes the cube wake. In $y0$, the cube presence impacts the cylinder wake and breaks the wake development: it significantly reduces l^*. Indeed, in the symmetry plane, $l^*_{y0} = 2.3$ for cases $C_1 2 C_6$ which is about three times lower than $l^*_{y0} = 6$ for case C_6.

Maps of $\overline{U}$ out of the symmetry plane (in $y1$ and $y2$) are presented in figure 14. In $y1$, the wake is not restored. However, in $y2$, the wake aspect downstream of the cylinder is similar to the wake past a cubic obstacle of aspect ratio between 1 and 6 [Martinuzzi and Tropea (1993)]. The lateral wake extension is here influenced by the cube presence for all the width with recirculation lengths always lower than for case C_6 at same transverse

position: $l^*_{y1} = 4.6$ and $l^*_{y2} = 4.1$.

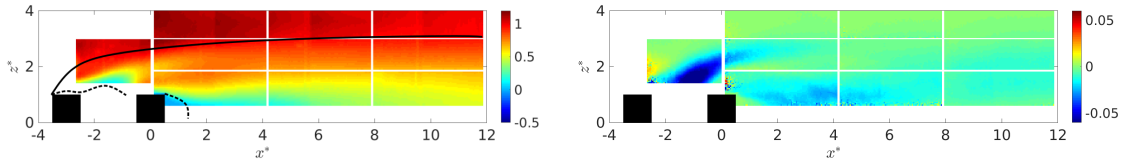

Figure 13: Average streamwise velocity $\overline{U}$ (left) and average Reynolds shear stress τ_{uw} (right) for case $C_1 2 C_6$ in $y0$. Full line is the wake extension ($\overline{U} = 0.9 * \overline{U}_\infty$) and dotted line marks out the recirculation area ($\overline{U} < 0$).

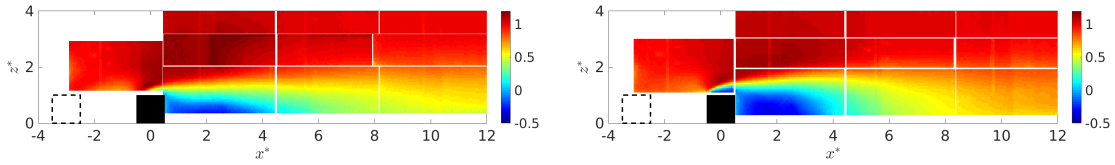

Figure 14: Average streamwise velocity $\overline{U}$ for case $C_1 2 C_6$ in $y1$ (left) and $y2$ (right).

Another combination case is considered with the positioning of 2 cubes and 2 cylinders. The flow behaviour around case $C_3 1 C_1^2 1 C_2$ is illustrated in figure 15(a) with average velocity fields in the symmetry plane and figure 15(b) with average Reynolds shear stress τ_{uw} maps. From $\overline{U}$ maps, recirculation length l^* can be evaluated. This length is defined as the distance between the middle of the downstream obstacle and the location where the flow reattaches downstream. Recirculation length downstream of the last obstacle, a cylinder of $A_R = 2$ is $l^* = 1.5$ which is weaker than $l^* = 3$ measured in [Martinuzzi and Tropea (1993)] for a single cylinder with identical A_R. The combination of wall-mounted elements reduces the recirculation length and consequently the wake. The average velocity perturbations ($\overline{U}_i nfty < 0.9$) and the shear stress ($\tau_{uw} < -0.02$) of the elements combination does not exceed $z^* = 2$ in altitude which is weak compared to the cube or cylinder alone cases.

4.2. Spectral analysis

Using LDV measurements, a spectral analysis is lead. PSD are plotted in figure 16 for case $C_1 2 C_6$ and for both available components u' and v' at various positions. In the spectrum, no specific peak is detectable. The

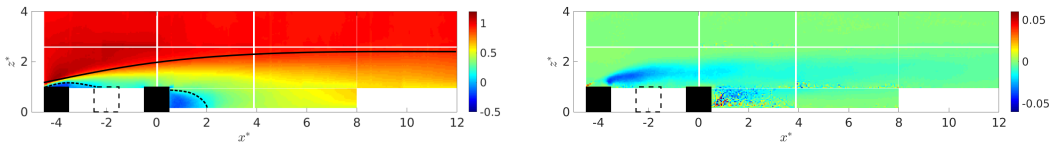

Figure 15: Average streamwise velocity $\overline{U}$ (left) and average Reynolds shear stress τ_{uw} (right) for case $C_3 1 C_1^2 1 C_2$ in $y0$. Full line is the wake extension ($\overline{U} = 0.9 * \overline{U}_\infty$) and dotted line marks out the recirculation area ($\overline{U} < 0$).

cube presence prevents the cylinder wake from developing and the periodic vortex shedding from happening due to strong impact of the turbulence and velocity deficit induced by the cube wake on the cylinder. Another aspect is the amplitude difference between PSD at $z^* = 1$ and $z^* = 4$: the highest the position, the furthest from the turbulent agitation in the wake. Indeed, velocity fluctuations u' and w' are higher in the wake than in the outer flow. For position $x^* = 11$, the wake extends between $z^* = 1$ and $z^* = 4$, hence both positions are located within the shear layer. At this position, the shear layer intensity is also lower. It results in spectra close for both altitudes at a lower amplitude compared to the maximal amplitude at $x^* = 1$ and $x^* = 5$. There is an energetic transfer from bottom to top in the streamwise direction as the shear layer evolves towards the free surface. Finally, we note that the spectrum of the two components are close at $z^* = 1$ as opposed to spectrum at $z^* = 4$. Overall, the spectrum are in good adequacy with the $-5/3$ slope.

4.3. Conclusion on obstacle combination cases

The addition of a cube upstream of a cylinder breaks the cylinder wake development and no structure energetic enough to rise up to the surface is detected. An obstacle combination generates a mean wake that does not rise in the water column nor extends in the streamwise direction compared to the cylinder case. It is expected that both cases are not critical for tidal turbines. That aspect is detailed in next section.

5. Critical flow events identification

In this section, the turbulence properties obtained from LDV and PIV measurements are presented in the symmetry plane $y0$ for four main cases: low and large aspect ratio cases of unitary obstacles: C_1 and C_L and for two obstacles combinations types: $C_3 1 C_1^2 1 C_2$ and $C_1 2 C_6$. It is shown in section

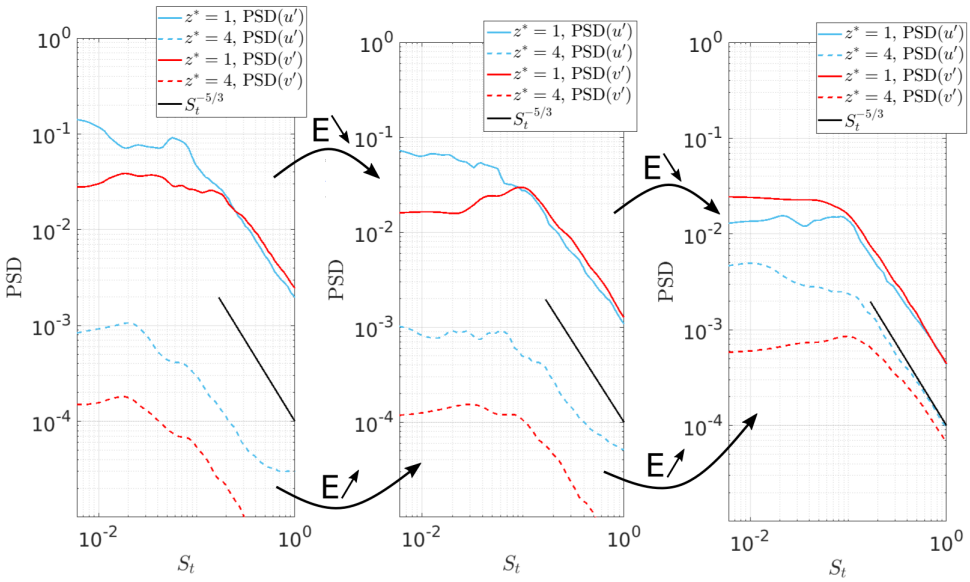

Figure 16: PSD spectrum of u' (blue) and v' (red) at $z^* = 1$ (−) and $z^* = 4$ (−−) for $x^* = 1$, $x^* = 5$ and $x^* = 11$ (left to right) for case $C_1 2 C_6$.

3.3 that the floor inclination gives an impulsion and it might cause a translation of the wake although it does not alter the turbulent events nature. This difference is not significant compared to the four cases considered and will not be investigated here.

5.1. Velocity profiles

In figure 17, velocity profiles are represented at four streamwise positions for the first 2 cases: $x^* = 1, 3, 10, 20$. In some cases, measurements were not performed for some streamwise positions or at specific height, hence the missing data in the figures. The comparison of cases C_1 and C_L illustrate, once again, the extension of the obstacle wake with the aspect ratio. C_1 profiles show a unperturbed flow above $z^* = 2.5$ with the 1.5 % turbulence intensity present in the incoming flow. Hence, the cube presence has no significant effect in the water column. C_L profiles show that, when close to the obstacle ($x^* = 1$ and $x^* = 3$), the profile is almost unperturbed above $z^* = 3$. Far from the obstacle ($x^* \geq 10$), strong fluctuations appear with a strong shear. For $x^* = 10$, maximal velocity fluctuations are obtained at $z^* = 2.5$: $U = 0.7 \pm 0.3 m/s$.

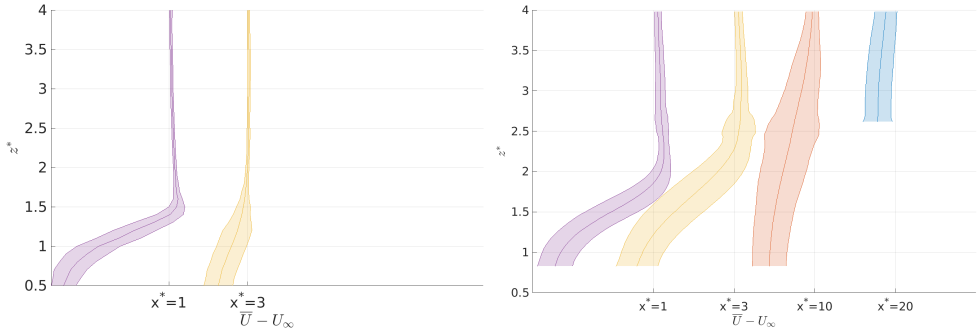

(a) C_1 case, LDV measurements

(b) C_L case, PIV measurements

Figure 17: $\overline{U}$ profiles for unitary cases surrounded by the standard deviation in the symmetry plane $y0$.

In figure 18, obstacles combinations are considered. Case $C_3 1 C_1^2 1 C_2$ shows profiles with few velocity fluctuations that appear only for $z^* < 3$. Above that altitude, the obstacles presence does not have any influence on the flow. As mentioned in section 4, this case is closer to a bottom roughness. Case $C_1 2 C_6$ shows that, close to the obstacle, the wake reaches higher altitudes compared to C_L case. However, profiles in the far wake of the obstacle are less turbulent in high altitudes ($z^* \geq 3$) since case $C_1 2 C_6$ wake extends significantly less compared to C_L. For $x^* = 10$, velocity fluctuations are at $z^* = 2.5$: $U = 0.9 \pm 0.1\ m/s$ for $C_1 1 C_1^2 1 C_3$ and $U = 0.8 \pm 0.2\ m/s$ for $C_1 2 C_6$.

Average streamwise velocity maps are used to schematically represent the wake expansion for each of the four cases in figure .24. This figure displays a representative wake extension by plotting the line corresponding to $\overline{U} = 0.9 \times U_\infty$. It also represents the limits of the recirculation area. The C_L case compared to other cases is the only one for which the wake reaches an altitude higher than $z^* = 3.5$. Both combination cases show a low rising angle wake unlike C_L wake which is directed towards the free surface, although the wake in case $C_1 2 C_6$ reaches higher altitude than case $C_3 1 C_1^2 1 C_2$. In case C_L, a boil, generated from the cylinder wake, is observed at the tank free surface, 32 H downstream of the cylinder (see picture 9). It is expected that C_L wake extends up to 32 H.

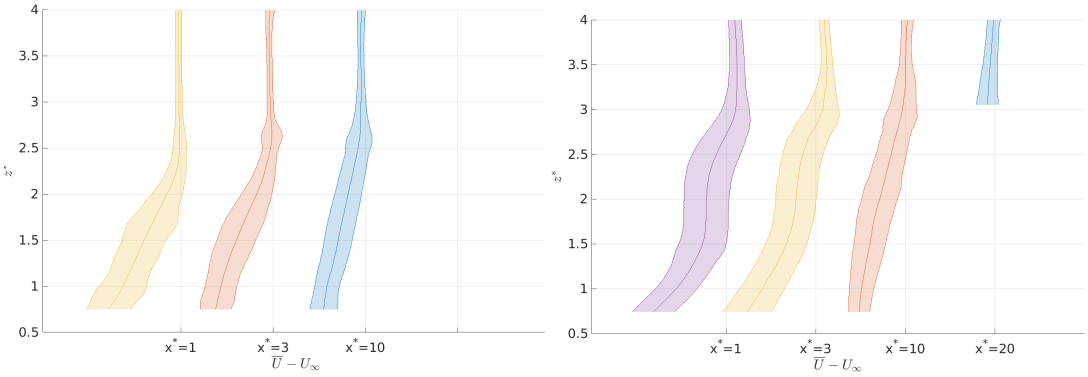

(a) $C_3 1 C_1^2 1 C_2$ case, PIV measurements

(b) $C_1 2 C_6$ case, PIV measurements

Figure 18: $\overline{U}$ profiles for combination cases surrounded by the standard deviation in the symmetry plane $y0$.

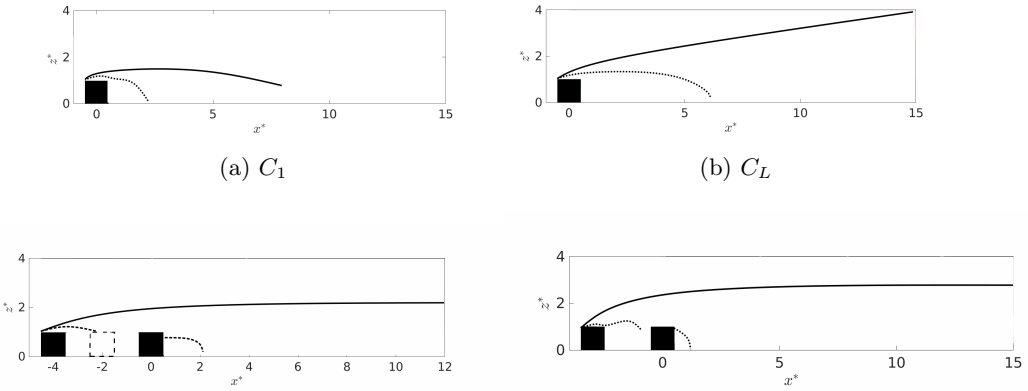

(a) C_1

(b) C_L

(c) $C_3 1 C_1^2 1 C_2$

(d) $C_1 2 C_6$

Figure 19: Schematic representation of the obstacles wake. Full line is the wake extension ($\overline{U} = 0.9 * \overline{U}_\infty$) and dotted line marks out the recirculation area ($\overline{U} < 0$).

5.2. Turbulent kinetic energy

2D Turbulent kinetic Energy (TKE) is defined in equation 1 using the streamwise and vertical fluctuating PIV velocity components. It gives an evaluation of the turbulent content produced downstream of an obstacle.

$$TKE = \frac{1}{2}\frac{(\sigma(u)^2 + \sigma(w)^2)}{\overline{U_\infty^2}} \tag{1}$$

TKE maps are plotted in figure 20 for the four cases considered. Case C_1 does not produce large amount of TKE and the disturbed area is substantially reduced compared to other cases. Results are within the range of those presented in [Yakhot et al. (2006)] on a cube, at $R_e = 6 \times 10^3$ in a low turbulence intensity flow, although their TKE is slightly stronger for $x^* > 1$, presumably due to the cut-off parts in-between planes that should contain most of the TKE. The presence of C_L in the flow produces a large layer of TKE that rises up to $z^* = 3$ and is directed towards the surface. It is also very intense, going up to $TKE = 0.12$. Results are similar to the study of [Panigrahi et al. (2008)] on a rib at Reynolds number 10 times weaker in a low turbulence intensity flow. For bottom roughness cases, energy is contained close to the obstacles. For case $C_3 1 C_1^2 1 C_2$, only a thin area above the first obstacle shows intense energy up to $TKE = 0.12$, that area does not exceed $z^* = 2$. For case $C_1 2 C_6$, as observed for the Reynolds shear stress, there is a large amount of TKE that is produced by the cube and impulsed by the cylinder up to $z^* = 3$. However, the extension of the area where $TKE > 0.05$ is less extended ($x^* < 6$) compared to C_L case.

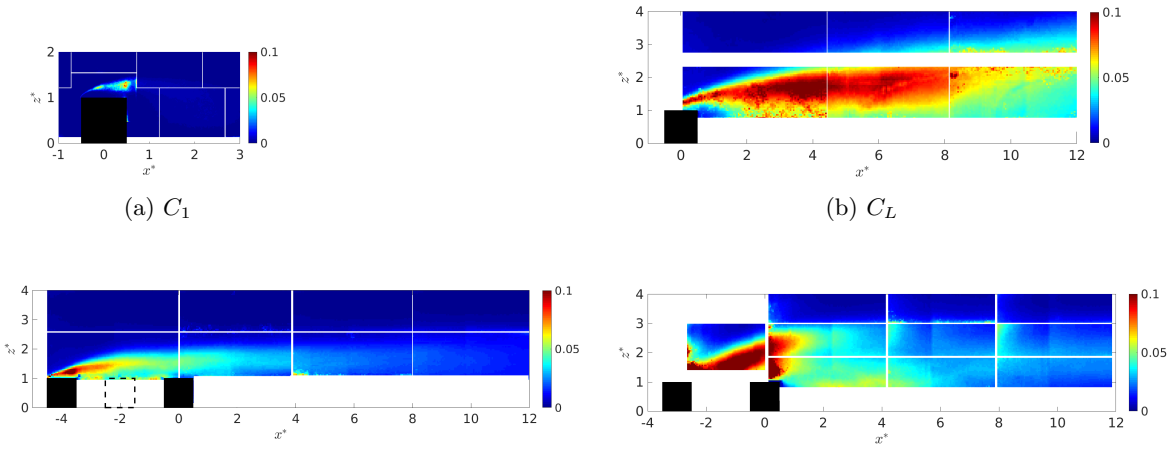

(a) C_1 (b) C_L

(c) $C_3 1 C_1^2 1 C_2$ (d) $C_1 2 C_6$

Figure 20: 2D Turbulent Kinetic Energy. White parts indicate non converged second order areas due to poor lightening.

To quantify the extension of turbulent perturbation in the wake, average Reynolds shear stress τ_{uw} and turbulent kinetic energy TKE are evaluated in the near and far wake ($x_s^* = 3$ and $x_s^* = 20$) for the 3 interesting test cases. For each case, a streamwise position is selected x_s^* and the altitude is chosen at mid-depth in the tank ($z_s^* = 4$). The energy is considered in a $0.5H \times 0.5\ H$ square around x_s^* and z_s^*. The data are temporally then spatially averaged on the surface considered. Results in table 3 show at $x_s^* = 3$ a Reynolds shear stress 4 times superior for C_L case compared to the other cases. TKE is around 2 times superior for C_L. In $x_s^* = 20$, results are closer although shear and turbulent intensity are still higher for C_L. We also note that, for case C_L: $|\tau_{uw}(x_s^* = 3)| > |\tau_{uw}(x_s^* = 20)|$ indicating the wake dissipation. However, for $C_1 2 C_6$: $|\tau_{uw}(x_s^* = 3)| < |\tau_{uw}(x_s^* = 20)|$ which could be a sign that the cube effect on the cylinder wake development decreases in the far wake. TKE levels are globally higher in the near wake than the far wake. It also worth mentioning that, in $x_s^* = 3$, τ_{uw} is higher for $C_3 1 C_1^2 1 C_2$ compared to $C_1 2 C_6$ although TKE is lower.

Case	$\lvert\tau_{uw}\rvert(x_s^* = 3)$ $\times 10^{-3}$	$TKE(x_s^* = 3)$ $\times 10^{-2}$	$\lvert\tau_{uw}\rvert(x_s^* = 20)$ $\times 10^{-3}$	$TKE(x_s^* = 20)$ $\times 10^{-2}$
C_L	10	4.7	9.0	3.9
$C_1 2 C_6$	1.6	2.9	3.8	2.8
$C_3 1 C_1^2 1 C_2$	3.1	2.0	X	X

Table 3: Average Reynolds shear stress τ_{uw} and turbulent kinetic energy TKE evaluated in a square around $z_s^* = 4$ and at $x_s^* = 3, 20$.

5.3. Large scale turbulent events

Previous sections showed that vortices are periodically shed in C_L and C_1 wake. In a previous study [Ikhennicheu et al. (2019b)], a method has been implemented to detect and track vortex centres using filtered PIV measurement for C_L case. The centre detection algorithm is not defined with any threshold value. However, that observation is submitted to the threshold chosen for the POD (*Proper Orthogonal Decomposition*) filter used to highlight the coherent structures in the flow [Ikhennicheu et al. (2019b)]. Additionally, vortex observation depends on the flow organisation. Applying the same methodology to all available database, it is observed that large turbulent events are only detected for cases C_L and $C_L S_6$, which are also the only cases where large boils can be observed at the free surface. Large

turbulent structures can be followed on each measurement plane independently (see figure 7(c)) since measurements are not simultaneous. All of the trajectories obtained for every measurement planes are represented in figure 21. In case C_L, additional measurement planes were performed for a more extensive analysis.

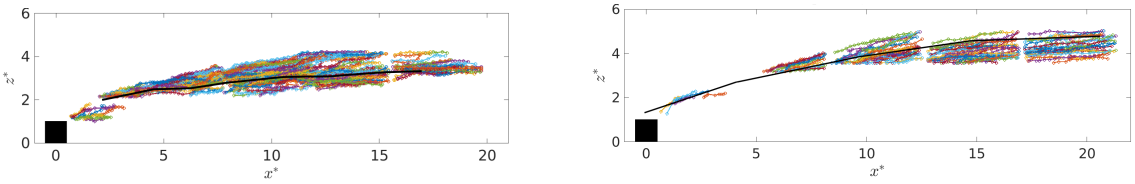

Figure 21: Vortices trajectories in the symmetry plane of case C_L (left) and $C_L S_6$ (right) (black line: top of the shear layer).

In [Ikhennicheu et al. (2019b)], it is explained that some of the trajectories have a higher rising angle as the one presented in figure 22. They show an horizontal radius 6 % inferior to average and a circulation 21 % higher than average in the measurement plane considered. Indeed, they are more elliptical and more energetic. These are later identified as 2D sections of larger 3D structures assimilated to hairpins structures.

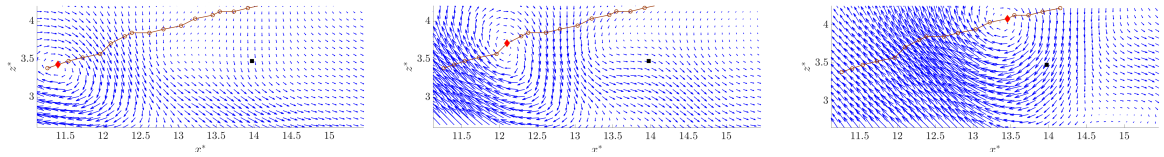

Figure 22: POD filtered velocity map of a vortex trajectory rising up between $t = 54.6$ and $t = 55.1$ s, case C_L, in the symmetry plane [Ikhennicheu et al. (2019b)]. Dot is the measurement point at which signals in figure 23 are extracted.

Fluctuating velocities u' and w' signals are plotted in figure 23 at a point taken in the middle of the measurement plane selected for figure 22. They show large velocity fluctuations correlated with the passing of large turbulent structures.

Among all of the cases presented here, these events are only visible for isolated large A_R obstacles. Other cases can show a shedding peak but no boil at the surface. Indeed, the detection algorithm developed in [Ikhennicheu et al. (2019b)] detects only a few events for other test cases. These events are low in energy. Authors suggest that, in order to generate large

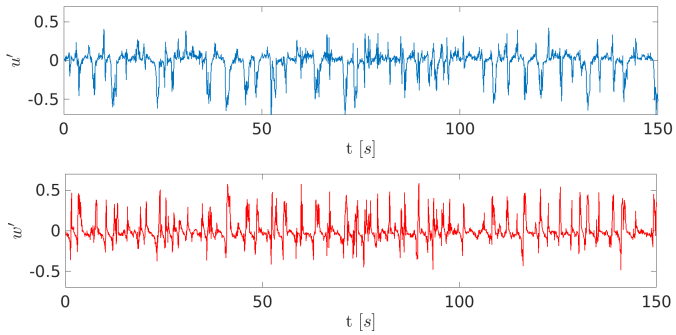

Figure 23: Signals of u' (top) and w' (bottom) at $(x^* = 14, y^* = 0, z^* = 3.5)$ for case C_L.

scale turbulent events, a large aspect ratio is needed (as confirmed by [Diabil et al. (2017)]). Additionally, the large A_R obstacle must be considered alone in the flow. Indeed, in case $C_1 2 C_6$, the cube presence induces perturbations in the cylinder wake that prevent large turbulent structures generation.

Results are summed up in table 4. The extension of the wake is described using δ_z^*, calculated as the boundary layer thickness : $\delta_z^* = z^*(\overline{U} = 0.95 \times \overline{U_\infty})$ in the wake of each obstacle combination. Its value is evaluated at each streamwise position and the maximal value is taken. In the table, for cases C_L and $C_L S_6$, the vertical extension of the wake is $8H = 2\ m = D_e$, the depth of the tank. Indeed, since large boils appear at the surface, it is assumed that the velocity fluctuations will reach the surface. In the case of $C_1 S_6$, as for the cylinder case, the wake is directed towards the free surface and extends higher than the measurement performed. However, fluctuations do not reach the surface. It is not possible to properly evaluate $\max(\delta_z^*)$. The value indicated ($\max(\delta_z^*)$=2) is measured at the furthest available measurement plane from the cube.

6. Conclusion and Perspectives

In this study, the question of large turbulent events generated by bathymetry variations is investigated. Bathymetry shows two types of topologies: a mean variation of $\sim 5\ m$ and unitary elements significantly more elevated ($\sim 10\ m$). The first is represented by combinations of wall-mounted cubic elements and the second by unitary wall-mounted cubic elements, with different aspect ratios. Using PIV and LDV measurements, the wake past

Case	l^*	$\max(\delta_z^*)$	S_t peak ($\times 10^{-2}$)	Boil at the surface
C_1	1.9	1.4	9	No
C_1S_6	1.7	> 2	9	No
C_L	6	8^*	6.5	Yes
C_LS_6	5.3	8^*	7.4	Yes
C_12C_6	2.3	2.7	No	No
C_3C1C_2	1.5	2.3	No	No

Table 4: Sum up of wake characteristics evaluated in the symmetry plane. An asterisk indicates that the associated length corresponds to the depth of the tank.

these test cases has been investigated.

The wake past obstacle combinations does not reach high altitudes and does not show large velocity fluctuations in the water column. PIV measurements out of the symmetry plane show that upstream obstacles have a significant influence on the obstacle wake. No specific peak can be identified by a spectral analysis.

Experiments on unitary small and large aspect ratio cases have been carried out. In the cylinder case, side effects do not impact the wake developing in the symmetry plane, hence the wake extends. A spatial analysis shows a peak consistent with periodic vortex shedding, for both cases. For the cube, these events are more frequent but they are smaller and do not persist in the flow, as opposed to the cylinder case where turbulent events reach the surface. The addition of an inclined floor downstream of the obstacle, consistent with smooth depth variation, gives an impulsion to the wake towards the free surface. Its presence induces a blocking effect that causes a squeezing of the wake which leads to the shear layer being thinner and shorter. For both the cube and the cylinder, the recirculation length reduces by 11 % with the addition of an inclined floor.

Finally, the impact of the four main test cases on the water column are compared: the cube, the cylinder and the two cases of obstacle combinations. The cylinder case shows the most extended wake and the profiles with the highest fluctuating velocities. Analysis show that some vortices that originate in the cylinder wake are very energetic and can rise up to the surface to create a boil. They have the size of a classical horizontal axis turbine and might be the most critical turbulent event impacting the blades

in terms of fatigue and power production. Additionally, a strong shear exists in the vertical profile and it can induce cyclic loads fluctuation. Based on the results of this study, recommendations for tidal turbine positioning are limited and additional studies are required. However, authors recommend avoiding areas where high and wide (perpendicularly to the flow) obstacles are present. The cube case will not impact the flow in the water column, and the combination cases stand between. Experiments were performed on the impact of the cylinder wake on an experimental turbine loads and behaviour and analysis are on-going [Gaurier et al. (2018)]. This whole set of experimental flow configurations aims also at constituting a database for numerical development [Mercier et al. (2017)].

7. Acknowledgment

This work benefits from a French State grant managed by the National Research Agency under the Investments for the Future program bearing the reference ANR-10-IEED-0006-11. The authors also acknowledge the financial support of Ifremer and the Hauts de France Regional Council for these PhD studies. This project was partly financially supported by the European Union (FEDER), the French government, IFREMER and the region Hauts-de-France in the framework of the project CPER 2015-2020 MARCO. We are grateful to the French navy SHOM ("Service Hydrographique et Océanographique de la Marine") for providing access to bathymetric data (http://data.shom.fr/). We are most grateful to Thomas Bacchetti, Inès Belarbi and Jean-Valery Facq for their assistance and precious advices.

Appendix: Test cases side and top view

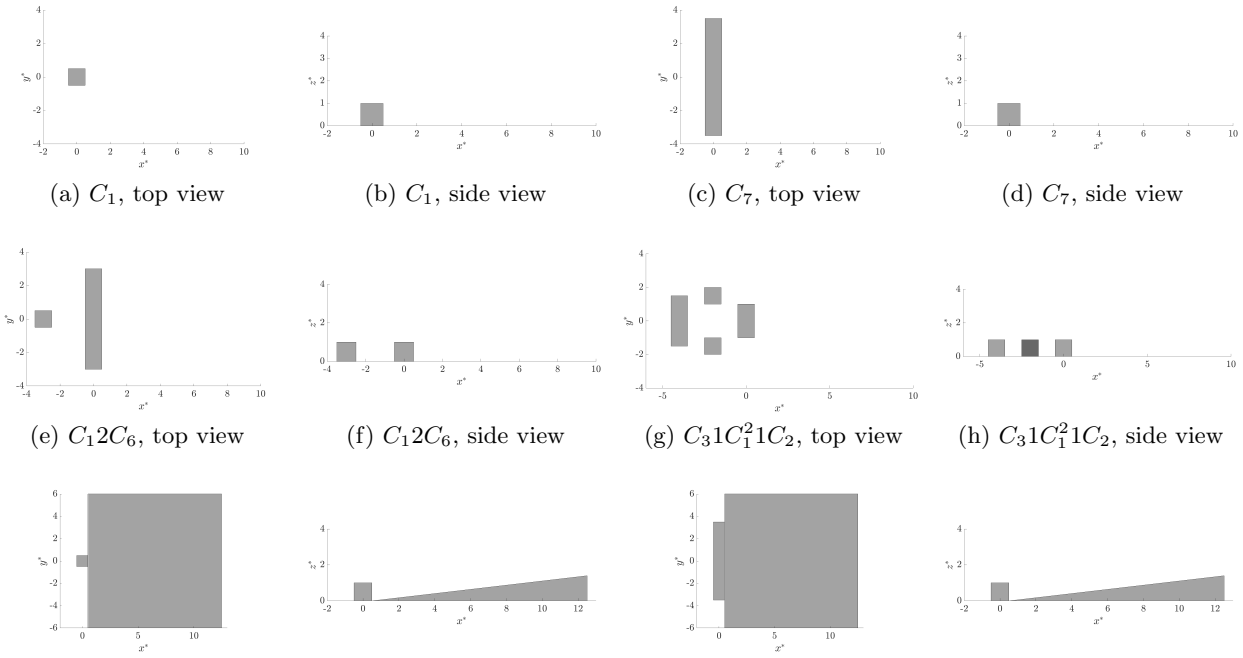

(a) C_1, top view (b) C_1, side view (c) C_7, top view (d) C_7, side view

(e) $C_1 2 C_6$, top view (f) $C_1 2 C_6$, side view (g) $C_3 1 C_1^2 1 C_2$, top view (h) $C_3 1 C_1^2 1 C_2$, side view

(i) $C_1 S_6$, top view (j) $C_1 S_6$, side view (k) $C_7 S_6$, top view (l) $C_7 S_6$, side view

Figure .24: Schematic representation of the obstacles from a top and side view.

References

R.J. Adrian and J. Westerweel. Particle image velocimetry. Cambridge University Press, Cambridge, 2011.

N. Beratlis, E. Balaras, and K. Squires. The role of surface texturing on the physics of boundary layer separation over a bump. Int. J. Heat Fluid Flow, 73:223–235, 2018.

J. Best. The fluid dynamics of river dunes: A review and some future research directions. J. Geophys. Res., 110, 2005.

I.P. Castro. Relaxing wakes behind surface-mounted obstacles in rough wall boundary layers. J. Fluid. Mech., 93:631–659, 1979.

I.P. Castro and A.G. Robins. The flow around a surface-mounted cube in uniform and turbulent streams. J. Fluid Mech., 79:307–335, 1977.

H.K. Chaurasia and M.C. Thompson. Three-dimensional instabilities in the boudary-layer flow over a long rectangular plate. J. Fluid Mech., 681: 411–433, 2011.

H. Choi, W.-P. Jeon, and J. Kim. Control of flow over a bluff body. Annu. Rev. Fluid Mech., 7340:113–139, 2008.

H.A. Diabil, X.K. Li, and I. E. Abdalla. Coherent structures and flow topology of transitional separated-reattached flow over two and three dimensional geometrical shapes. Mathematical Methods and Computational Techniques in Science and Engineering- AIP Conference proceedings, 020019, 2017.

O. Duràn Medina, F.G. Schmitt, R. Calif, G. Germain, and B. Gaurier. Correlation between synchronised power and flow measurements, a way to characterize turbulent effects on a marine current turbine. EWTEC, Nantes, France, 2015.

O. Duràn Medina, F.G Schmitt, R. Calif, G. Germain, and B. Gaurier. Turbulence analysis and multiscale correlations between synchronized flow velocity and marine turbine power production. Renew. Energ., 112:314–327, 2017.

EDF. Énergies marines hydrolienne et houlomotrice. Conférence institut Coriolis, 2010.

E. Florens, O. Eiff, and F. Moulin. Defining the roughness sublayer and its turbulent statistics. Exp. Fluids, 54:1–15, 2013.

B. Gaurier, P. Davies, A. Deuff, and G. Germain. Flume tank characterization of marine current turbine blade behaviour under current and wave loading. Renew. Energ., 59:1–12, 2013.

B. Gaurier, M. Ikhennicheu, Ph. Druault, G. Germain, J.-V. Facq, and G. Pinon. Experimental study of the wake of a wide wall-mounted obstacle on the behaviour of a marine current turbine. Journée de l'Hydrodynamique, Marseille, France, 2018.

R. J. Hearst, G. Gomit, and B. Ganapathisubramani. Effect of turbulence on the wake of a wall-mounted cube. J. Fluid Mech., 804:513–530, 2016.

H.J. Hussein and R.J. Martinuzzi. Energy balance for turbulent flow around a surface mounted cube placed in a channel. Phys. Fluids, 8:764–780, 1996.

M. Ikhennicheu, B. Gaurier, Ph. Druault, and G. Germain. Experimental analysis of the floor inclination effect on the turbulent wake developing behind a wall mounted cube. Eur. J. Mech. B/Fluid, 72:340–352, 2018a.

M. Ikhennicheu, G. Germain, B. Gaurier, and Ph. Druault. Experimental study of the wake past cubic wall-mounted elements to predict flow variations for tidal turbines. AWTEC, Taipei, Taiwan, 2018b.

M. Ikhennicheu, B. Gaurier, G. Germain, Ph. Druault, G. Pinon, and J.-V. Facq. Experimental study of the wall-mounted cylinder wake effects on a tidal turbine behaviour compared to free stream turbulence. Proceedings of the 13th European Wave and Tidal Energy Conference, Napoli, Italy, 2019a.

M. Ikhennicheu, G. Germain, Ph. Druault, and B. Gaurier. Experimental study of coherent flow structures past a wall-mounted square cylinder. Ocean Engineering, 182:137–146, 2019b.

J. Jiménez. Turbulent flows over rough walls. Annu. Rev. Fluid Mech., 36: 173–96, 2004.

T. Leweke, S. Le Dizès, and C.H.K. Williamson. Dynamics and instabilities of vortex pairs. Annu. Rev. Fluid Mech., 37:59–80, 1999.

H.C. Lim, I.P. Castro, and R.P. Hoxey. Bluff bodies in deep turbulent boundary layers: Reynolds-number issus. J. Fluid Mech., 570:97–118, 2007.

Y.Z. Liu, F. Ke, and H.J. Sung. Unsteady separated and reattaching turbulent flow over a two-dimensional square rib. J. Fluid Struct., 24:366–381, 2008.

J. Martinuzzi and B. Havel. Turbulent flow around two interfering surface-mounted cubic obstacles in tandem arrangement. J. Fluid Eng., 122: 24–31, 2000.

R. Martinuzzi and C. Tropea. The flow around surface-mounted, prismatic obstacles placed in a fully developed channel flow, *(Data Bank Contribution)*. J. Fluid Eng., 115:85–92, 1993.

C.D. Meinhart, A.K. Prasad, and R.J. Adrian. A parallel digital processor system for particle image velocimetry. Meas. Sci. Technol., 4:619–626, 1993.

M. Mercier, M. Grondeau, S. Guillou, J. Thiébot, and E. Poizot. Towards the modelling of turbulence at tidal stream power sites with the lattice boltzmann method. EWTEC, Cork, Ireland, 2017.

A. Muller and A. Gyr. On the vortex formation in the mixing layer behind dunes. J. Hydraul. Res., 24:359–375, 1987.

P. Mycek, B. Gaurier, G. Germain, G. Pinon, and E. Rivolaen. Experimental study of the turbulence intensity effects on marine current turbines behaviour. Part I: One single turbine. Renew. Energ., 66:729–746, 2014.

L. Myers and A. Bahaj. Simulated electrical power potential harnessed by marine current turbine arrays in the Alderney Race. Renew. Energ., 30: 1713–1731, 2005.

M. Omidyeganeh and U. Piomelli. Large-eddy simulation of two-dimensional dunes in a steady, unidirectional flow. J. Turbul., 42:1–31, 2011.

J. Paik, F. Sotiropoulos, and F. Porté-Agel. Detached eddy simulation of flow around two wall-mounted cubes in tandem. Int. J. heat Fluid Fl., 30: 286–305, 2009.

P.K. Panigrahi, A. Schroeder, and J. Kompenhans. Turbulent structures and budgets behind permeable ribs. Exp. Therm. Fluid Science, 32:1011–1033, 2008.

S.B. Pope. Turbulent flows. Cambridge University Press, Cambridge, 2000.

H. Sakamoto and H. Haniu. Effect of free-stream turbulence on characteristics of fluctuating forces acting on two square prisms in tandem arrangement. J. Fluid Eng., 110:140–146, 1988.

W.H. Schofield and E. Logan. Turbulent shear flow over surface mounted obstacles. J. Fluid Eng., 112:376–385, 1990.

SHOM. MNT bathymétrique de façade atlantique (projet homonim). 2015.

S. K. Singh, K. Debnath, and B. S. Mazumder. Spatially-averaged turbulent flow over cubical roughness in wave-current co-existing environment. Costal Eng., 114:77–85, 2016.

R.J. Volino, M.P. Schultz, and K.A. Flack. Turbulence structure in boundary layers over periodic two- and three-dimensional roughness. J. Fluid Mech., 676:172–190, 2009.

L. Wang, M. Salewski, and B. Sundén. Turbulent flow in a ribbed channel: Flow structures in the vicinity of a rib. Exp. Therm. Fluid Sci., 34(2): 165–176, 2009.

J. Westerweel and F. Scarano. Universal outlier detection for PIV data. Exp. Fluids, 39:1096–1100, 2005.

A. Yakhot, H. Liu, and N. Nikitin. Turbulent flow around a wall-mounted cube: A direct numerical simulation. Int. J. Heat Fluid Fluid, 27:994–1009, 2006.